Using the motion of S2 to constrain scalar clouds around Sgr A*

Foschi, A.; Abuter, R.; Aimar, N.; Amaro Seoane, P.; Amorim, A.; Bauböck, M.; ... ; Yazici, S.

Using the motion of S2 to constrain scalar clouds around Sgr A*

A. Foschi [1,2]★ R. Abuter,[3] N. Aimar,[4] P. Amaro Seoane,[5,6,7,8] A. Amorim,[1,9] M. Bauböck,[6,10]
J.P. Berger [11] H. Bonnet,[3] G. Bourdarot,[6] W. Brandner [12] V. Cardoso,[1,13]★ Y. Clénet,[4] Y. Dallilar,[6]
R. Davies,[6] P.T. de Zeeuw,[14] D. Defrère,[15] J. Dexter,[16] A. Drescher,[6] A. Eckart,[17,18] F. Eisenhauer,[6]
M.C. Ferreira,[1] N.M. Förster Schreiber,[6] P.J.V. Garcia,[1,2]★ F. Gao,[6,19] E. Gendron,[6] R. Genzel,[6,20]
S. Gillessen,[6] T. Gomes,[1,2] M. Habibi,[6] X. Haubois,[21] G. Heißel,[4,22] T. Henning,[12] S. Hippler,[12]
S.F. Hönig,[23] M. Horrobin,[17] L. Jochum,[21] L. Jocou,[11] A. Kaufer,[21] P. Kervella,[4] L. Kreidberg,[12]
S. Lacour,[4] V. Lapeyrère,[4] J.-B. Le Bouquin,[11] P. Léna,[4] D. Lutz,[6] F. Millour,[24] T. Ott,[6] T. Paumard,[4]
K. Perraut,[11] G. Perrin,[4] O. Pfuhl,[3,6] S. Rabien,[6] D.C. Ribeiro,[6] M. Sadun Bordoni,[6] S. Scheithauer,[12]
J. Shangguan,[6] T. Shimizu,[6] J. Stadler,[6,25] O. Straub,[6,26] C. Straubmeier,[17] E. Sturm,[6] C. Sykes,[23]
L.J. Tacconi,[6] F. Vincent,[4] S. von Fellenberg,[6,18] F. Widmann,[6] E. Wieprecht,[6] E. Wiezorrek,[6] J. Woillez[3]
and GRAVITY Collaboration[13,17]†

Affiliations are listed at the end of the paper

ABSTRACT

The motion of S2, one of the stars closest to the Galactic Centre, has been measured accurately and used to study the compact object at the centre of the Milky Way. It is commonly accepted that this object is a supermassive black hole, but the nature of its environment is open to discussion. Here, we investigate the possibility that dark matter in the form of an ultralight scalar field 'cloud' clusters around Sgr A*. We use the available data for S2 to perform a Markov Chain Monte Carlo analysis and find the best-fit estimates for a scalar cloud structure. Our results show no substantial evidence for such structures. When the cloud size is on the order of the size of the orbit of S2, we are able to constrain its mass to be smaller than 0.1 % of the central mass, setting a strong bound on the presence of new fields in the galactic centre.

Key words: black holes physics – dark matter – gravitation – celestial mechanics – Galaxy: centre.

1 INTRODUCTION

The orbit of the star S2 in the Galactic Centre (GC) has been monitored for almost 30 years with both spectroscopic and astrometric measurements, the latter reaching a precision of $\approx 50\,\mu$as since the GRAVITY instrument at the Very Large Telescope Interferometer (VLTI) has been put into operation (GRAVITY Collaboration 2017). S2 is a star with mass around 10–15 $M_\odot$ orbiting Sgr A* with a period of roughly 16 years and apparent magnitude $K \sim 14$ (Ghez et al. 2003; Habibi et al. 2017). It is part of the so-called Sagittarius A* cluster, consisting of about 40 stars, known as S-stars, whose orbits are all located within one arcsecond distance from Sgr A*(Eckart & Genzel 1996; Schödel et al. 2002; Ghez et al. 2003; Gillessen et al. 2009a, b; Sabha et al. 2012). The data collected has allowed constraining

with unprecedented accuracy both the mass M of the central object and the GC distance R_0. In particular, the trajectory of the S2 star, together with those of other stars in the S-cluster, showed that their motion is determined by a potential generated by a dark object with mass $M \sim 4.3 \cdot 10^6\,M_\odot$ at a distance $R_0 \sim 8.3$ kpc (Ghez et al. 2008; GRAVITY Collaboration 2019b, 2022), widely believed to be a supermassive black hole (SMBH, Genzel et al. 2010, Eisenhauer & Gillessen 2010). This hypothesis has been supported by the direct observations of near-IR flares in the relativistic accretion zone of Sgr A*, corresponding to the innermost stable circular orbit of a black hole (BH) (GRAVITY Collaboration 2018b), and, most recently, analysing the image of Sgr A* taken by the Event Horizon Telescope (EHT), which is compatible with the expected appearance of a Kerr BH with such a mass (Akiyama et al. 2022).

While the nature of the central object seems to be well established, its surrounding environment remains mostly unknown. In this context, an especially exciting prospect is that dark matter (DM) may cluster around supermassive BHs, producing spikes in the local density (Gondolo & Silk 1999; Sadeghian 2013, Ferrer & Will 2013), leaving imprints in the orbits of stars. The scattering of DM by passing stars or BHs, or accretion by the central BH induced by heating in its vicinities may significantly soften the spike distribution

★ E-mail: arianna.foschi@tecnico.ulisboa.pt (AF); vitor.cardoso@tecnico.ulisboa.pt (VC); pgarcia@fe.up.pt (PJV)

(Merritt et al. 2002; Merritt 2004; Bertone & Merritt 2005). Given the outstanding challenge that DM represents, it is specially important to test the presence of new forms of matter in the GC (for a review on the GC and how it can be used to constrain DM see de Laurentis et al. 2022).

Data collected for S2 has been used to test the presence of an extended mass within its apocenter ($r_{\rm apo,S2} = 14$ mas) with particular attention to spherically symmetric DM density distributions (see e.g. Lacroix (2018); Bar et al. (2019); GRAVITY Collaboration (2022); Heißel et al. (2022)).

Lacroix (2018) used data up to 2016 to fit the size of a DM spike within a halo described by a density profile (Zhao 1996):

$$\rho_{\rm NFW} = \rho_{\rm s} \left(\frac{r}{r_{\rm s}}\right)^{-\gamma} \left(1 + \frac{r}{r_{\rm s}}\right)^{\gamma-3}, \tag{1}$$

where $r_{\rm s}$ is the scale radius, $\rho_{\rm s}$ is the scale density, which can be trivially related to the local DM density. Lacroix was able to exclude a spike with a radius greater than 10^3 pc (Fig. 2, last plot), which corresponds to $R_{\rm sp} \approx 4.8 \cdot 10^9\, M$, which can be translated in an upper bound on the total 'environmental' mass δM within the characteristic size of the orbit, $\delta M \lesssim 4$–$5 \cdot 10^4\,{\rm M}_\odot$, i.e. $\sim 1\%\, M$.

Bar et al. (2019) used similar data to constrain the presence of ultralight dark matter, i.e. matter in the form of a self-gravitating scalar condensate. This assumption fixes the density distribution of the mass profile, and they were able to set an upper bound on the soliton mass of $\delta M \sim 5 \cdot 10^4\,{\rm M}_\odot$ for a fundamental scalar field with mass $m_{\rm s} \sim 4 \cdot 10^{-19}$ eV. For $m_{\rm s} \gtrsim 10^{-18}$ eV, the soliton is confined inside S2 periastron and is degenerate with the BH mass.

Della Monica & de Martino (2023) used a similar procedure to derive an upper limit of $< 10^{-19}$ eV on the mass of ultralight boson to beat 95% confidence level.

Recently, GRAVITY Collaboration (2022) provided the current 1σ upper bound on the environmental mass δM within the orbit of S2, namely $\delta M \sim 4000\,{\rm M}_\odot$, or 0.1% of the BH mass. This limit was obtained assuming a Plummer model for the matter profile,

$$\rho_{\rm Plummer} = \frac{3 f_{\rm PL} M}{4\pi a_0^3} \left(1 + \left(\frac{r}{a_0}\right)^2\right)^{-5/2}, \tag{2}$$

with a_0 a length scale of the external matter distribution, which has mass $f_{\rm PL} M$. In fact, considering a scale length given by roughly S2's apoastron ($a_0 = 0.3$ arcsec), a best-fitting value for a fraction of extended mass within S2's orbit of $f_{\rm PL} = (2.7 \pm 3.5) \cdot 10^{-3}$ was found, i.e. $f_{\rm PL}$ is compatible with zero at 1σ confidence level, and it can be interpreted as a null result. Using, in addition, the orbits of the other four S-stars, upper limits on the extended mass were imposed, of order $10^3\,{\rm M}_\odot$, equivalent to 0.1% of the central mass M.

Thus far, the profile of the matter distribution has been mostly ad hoc. Here, we study the possibility that new fundamental fields exist and that they 'condense' in a bound state around the BH (for a review, see Brito, Cardoso & Pani (2015b)). These fields might be a significant component of dark matter or simply as-yet unobserved forms of matter. It is a tantalizing possibility that supermassive BHs might then be used as particle detectors, a possibility that we explore, using the motion of S2 as a probe of the matter content. In this context, the matter profile is known and given by the spatial profile of bound states around spinning BHs (Detweiler 1980; Cardoso & Yoshida 2005; Dolan 2007; Witek et al. 2013; Brito et al. 2015b). It can be argued that also in the context of fuzzy dark matter, composed of an ultralight scalar, the near-horizon region is controlled by BH physics and hence governed by the same type of profile we consider here (Cardoso et al. 2022b). The suggestion that the stars' motion can be

used to probe light fields around BHs is not new (Cardoso et al. 2011; Ferreira et al. 2017; Fujita & Cardoso 2017), but is here explicitly explored with data from the GRAVITY instrument.

2 THE SET-UP

Light bosonic fields can arise in a variety of contexts, for example, in string-inspired theories (Arvanitaki et al. 2010). However, early examples arose out of the need to explain in a natural way the smallness of the neutron electric dipole moment. They invoked the existence of a new axionic, light, degree of freedom (Peccei & Quinn 1977; Weinberg 1978; Wilczek 1978; Abbott & Sikivie 1983; Dine & Fischler 1983; Preskill et al. 1983).

In the presence of a spinning BH, small fluctuations of a massive scalar field can be exponentially amplified via superradiance, leading to a condensate – a bound state – outside the horizon (Brito et al. 2015b). This structure can carry up to $\sim 10\%$ of the BH mass if grown in a vacuum. It is also possible that the scalar soliton existed on its own, for example, if it is part of dark matter, in which case the placing of a BH at its centre will lead to a long-lived structure (a 'cloud') that on BH scales resembles the superradiant bound states (Cardoso et al. 2022a, b). Here, we will be agnostic regarding the origin of the scalar structure, but we will use our knowledge about the spatial profile of bound states around BHs.

2.1 The scalar field profile

Consider a particle moving in a potential given by a central mass M surrounded by a scalar field cloud. Our starting point is the set-up developed in GRAVITY Collaboration (2019a), and here we recall the most relevant steps of their procedure.

A system composed of a central BH with mass M and a scalar field minimally coupled to gravity is described by the action

$$S = \int d^4x \sqrt{-g} \left(\frac{R}{16\pi G} - \frac{1}{2} g^{\alpha\beta} \psi_{,a}^* \psi_{,b}^* - \frac{\mu^2}{2} \psi \psi^*\right), \tag{3}$$

where R is the Ricci scalar, $g_{\mu\nu}$ and g are the metric and its determinant. We assume that the BH spins along the z-axis, with adapted spherical coordinates (t, r, θ, ϕ), with $\theta = \pi/2$ defining the equator. The scalar $\psi(t, r, \theta, \phi)$ is a complex field, and μ is a mass parameter for the scalar field. It is related to the physical mass $m_{\rm s}$ via $\mu = m_{\rm s} c/\hbar$ and to the (reduced) Compton wavelength of the particle via $\lambda_C = \mu^{-1}$. The principle of least action results in the Einstein–Klein–Gordon system of equations, where the energy-momentum tensor of the scalar field can be written as

$$T_{\mu\nu} = \frac{1}{2} \left[\psi_{,\mu} \psi_{,\nu}^* + \psi_{,\nu} \psi_{,\mu}^* - g_{\mu\nu}\left(\psi^{,\sigma} \psi_{,\sigma}^* + \mu^2 |\psi|^2\right)\right]. \tag{4}$$

In the low-energy limit, i.e. neglecting terms of $\mathcal{O}(c^{-4})$, the energy density of the field reads

$$\rho = \frac{m_{\rm s}^2 c^2}{\hbar^2} |\psi|^2 = \mu^2 |\psi|^2 = \left(\frac{\alpha}{M}\right)^2 |\psi|^2, \tag{5}$$

where we have defined the dimensionless mass coupling α as

$$\alpha = \left[\frac{GM}{c^2}\right] \left[\frac{m_{\rm s} c}{\hbar}\right]. \tag{6}$$

From now on, we will use natural units ($G = c = \hbar = 1$) unless otherwise stated.

The solution of the Klein–Gordon equation for the field ψ on a Kerr background can be decomposed into a radial and an angular part, as $\psi = e^{-i\omega t + im\phi} S_{lm}(\theta) R_{lm}(r)$, where l, m are the angular modes, and
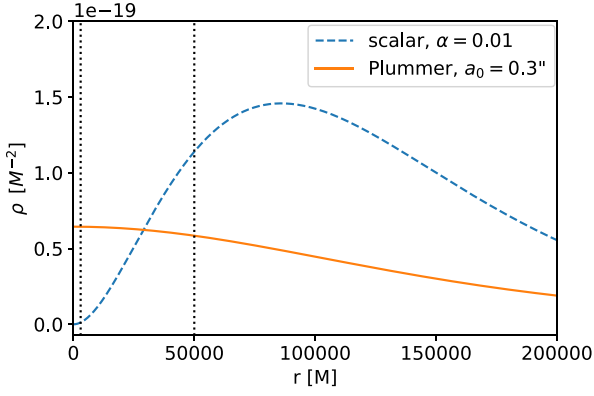
Figure 1. Comparison between the scalar field density in equation (5) with $\alpha = 0.01$, $\Lambda = 10^{-3}$, and $\theta = \pi/2$ (blue-dashed line) and the Plummer density in equation (2) with $a_0 = 0.3$ arcsec and $f_{\rm PL} = 10^{-3}$ (orange solid line). Black-dotted lines correspond to S2's periastron ($r_{\rm peri} \sim 3000\,M$) and apoastron ($r_{\rm apo} \sim 50\,000\,M$).

$\omega \sim \mu$ defines the frequency of the field. In the limit of small coupling ($\alpha \ll 1$), the radial part is proportional to the generalised Laguerre polynomials L_n^{2l+1} and the angular part becomes $S_{lm}(\theta) = P_l^m(\cos \theta)$ with $P_l^m(\cos \theta)$ being the associated Legendre polynomials. In this approximation, the fundamental mode $n = 0, l = m = 1$ of the scalar field is given by (Brito et al. 2015a)

$$\psi = A_0 e^{-i(\omega t - \phi)} \frac{r}{M} \alpha^2 e^{-\frac{r\alpha^2}{M}} \sin \theta, \tag{7}$$

where the amplitude of the field A_0 is related to the mass of the cloud via

$$M_{\rm cloud} = \int \rho s^2 \sin \theta \, \mathrm{d}\theta \, \mathrm{d}s \, \mathrm{d}\phi = \frac{64\pi A_0^2}{\alpha^4} M. \tag{8}$$

We can now use the energy density of the field to solve Poisson's equation $\nabla^2 U_{\rm sca} = 4\pi \rho$, using the usual harmonic decomposition implemented in Poisson & Will (2014), i.e. expanding all quantities in spherical harmonics $Y_{lm} = Y_{lm}(\theta, \phi)$. For the energy density computed in (5), the only non-zero terms that contribute to the scalar potential are the $l = m = 0$ and $l = 2$, $m = 0$ terms, resulting in a potential given by

$$U_{\rm sca} = 4\pi \left[\frac{q_{00}}{r} Y_{00} + p_{00} Y_{00} \right] + \frac{4\pi}{5} \left[\frac{q_{20}}{r^3} Y_{20} + p_{20} r^2 Y_{20} \right]$$
$$= \Lambda \left(P_1(r) + P_2(r) \cos^2 \theta \right), \tag{9}$$

where $\Lambda = M_{\rm cloud}/M$ is the fractional mass of the scalar field cloud to the BH mass,

$$P_1(r) = \frac{M}{r} + \frac{3M^3}{r^3 \alpha^4} - \frac{e^{-\frac{r\alpha^2}{M}}}{16 M^2 r^3 \alpha^4} \left(48 M^5 + 48 M^4 r \alpha^2 + 40 M^3 r^2 \alpha^4 \right.$$
$$\left. + 20 M^2 r^3 \alpha^6 + 6 M r^4 \alpha^8 + r^5 \alpha^{10} \right), \tag{10}$$

and

$$P_2(r) = -\frac{9M^3}{r^3 \alpha^4} + e^{-\frac{r\alpha^2}{M}} \left(\frac{9M}{2r} + \frac{9M^3}{r^3 \alpha^4} + \frac{9M^2}{r^2 \alpha^2} \right.$$
$$\left. + \frac{3\alpha^2}{2} + \frac{3r\alpha^4}{8M} + \frac{r^2 \alpha^6}{16 M^2} \right). \tag{11}$$

In Fig. 1, we show the difference between the scalar field density in (5) along the equator ($\theta = \pi/2$, with $\Lambda = 10^{-3}$ and $\alpha = 0.01$) and the density given by a Plummer profile (2), where we use the same values as in GRAVITY Collaboration (2022): $a_0 = 0.3$ arcsec and $f_{\rm PL} = 10^{-3}$.

GRAVITY Collaboration (2019a) showed that a scalar field cloud described by the potential (9) can leave imprints in the orbital elements of S2 if its mass coupling constant is in the range

$$0.005 \lesssim \alpha \lesssim 0.05, \tag{12}$$

assuming a fixed direction of the BH spin axis with respect to the plane of the sky, which corresponds to an effective mass of the field in the range $10^{-20}\,\mathrm{eV} \lesssim \mu \lesssim 10^{-18}\,\mathrm{eV}$. However, Kodama & Yoshino (2012) showed that for an SMBH with the mass of Sgr A*, the allowed range of effective masses that can engage a superradiant instability on a time-scale smaller than the cosmic age is $10^{-18}\,\mathrm{eV} \lesssim \mu \lesssim 10^{-15}\,\mathrm{eV}$. Hence, if a cloud exists and leaves detectable imprints in the orbit of S2, then its formation and existence must be explained by means of a different physical process, as discussed in Section 2. However, since the variations in the orbital elements induced by the cloud are potentially detectable with the current precision of the GRAVITY instrument, it is worth comparing these theoretical expectations with the available data. In particular, we are interested in fitting the fractional mass of the cloud $\Lambda = M_{\rm cloud}/M$ to a fixed value of the mass coupling constant α.

2.2 The equations of motion

To obtain the equations of motion of a particle moving in a central potential plus the toroidal scalar field distribution described by (7), we started from the Lagrangian

$$\mathfrak{L} = \frac{1}{2}(\dot{r}^2 + r^2 \dot{\theta}^2 + r^2 \sin^2 \theta \dot{\phi}^2) + U(r, \theta), \tag{13}$$

where

$$U(r, \theta) = \frac{M}{r} + \Lambda \left(P_1(r) + P_2(r) \cos^2 \theta \right), \tag{14}$$

is the sum of the Newtonian and the scalar potential. Solving the Euler–Lagrange equations translates into having the following equations of motion,

$$\ddot{r} = -\frac{M}{r^2} + r(\dot{\theta}^2 + \sin^2 \theta \dot{\phi}^2) + \Lambda \left(P_1'(r) + P_2'(r) \cos^2 \theta \right)$$
$$\ddot{\theta} = \cos \theta \sin \theta \dot{\phi}^2 - \frac{2}{r}\dot{r}\dot{\theta} - \frac{\Lambda P_2(r) \sin 2\theta}{r^2}$$
$$\ddot{\phi} = -\frac{2\dot{\phi}}{r}(\dot{r} + \cot \theta \, r \dot{\theta}), \tag{15}$$

where the prime (dot) indicates a derivative with respect to the radial (time) coordinate. Since the Schwarzschild precession has been detected in the orbit of S2 at 7σ confidence level (GRAVITY Collaboration 2022), we also included the first Post Newtonian correction in the equations of motion. The acceleration term is given by (Will 2008)

$$\boldsymbol{a}_{\rm 1PN} = f_{\rm SP} \frac{M}{r^2} \left[\left(\frac{4M}{r} - v^2 \right) \frac{\boldsymbol{r}}{r} + 4\dot{r}\boldsymbol{v} \right], \tag{16}$$

where $\boldsymbol{r} = r\hat{r}$,

$$\boldsymbol{v} = (\dot{r}\hat{r}, r\dot{\theta}\hat{\theta}, r\dot{\phi}\sin \theta \hat{\phi}), \tag{17}$$

and $v = |\boldsymbol{v}|$. Here, we have also introduced the dimensionless parameter $f_{\rm SP}$ that quantifies the Schwarzschild precession, and it is found to be $f_{\rm SP} = 0.99 \pm 0.15$ (GRAVITY Collaboration 2022). In this work, we fixed $f_{\rm SP} = 1$.

If we impose $\Lambda = 0$ and $f_{\rm SP} = 0$, we recover the classical motion of a particle orbiting a central point mass. The six initial conditions

for the set of equations in (15) can be obtained from the analytical solution of the Keplerian two-body problem, namely

$$r_0 = \frac{a_{\text{sma}}(1 - e^2)}{1 + e \cos \phi_0}, \qquad \dot{r}_0 = \frac{2\pi e a_{\text{sma}} \sin \mathcal{E}}{P(1 - e \cos \mathcal{E})}$$

$$\theta_0 = \frac{\pi}{2} \qquad \qquad \dot{\theta} = 0 \qquad (18)$$

$$\phi_0 = 2 \arctan\left(\sqrt{\frac{1 + e}{1 - e}} \tan \frac{\mathcal{E}}{2}\right) \qquad \dot{\phi}_0 = \frac{2\pi(1 - e)}{P(e \cos \mathcal{E} - 1)^2} \sqrt{\frac{1 + e}{1 - e}},$$

where e, a_{sma}, P are the eccentricity, the semimajor axis and the period of the orbit, respectively, while $\mathcal{E}$ is the eccentric anomaly evaluated from Kepler's equation: $\mathcal{E} - e \sin \mathcal{E} - \mathcal{M} = 0$, where $\mathcal{M} = n(t - t_{\text{p}})$ is the mean anomaly, $n = 2\pi/P$ is the mean angular velocity and t_{p} is the time of periastron passage. Details about how we performed the numerical integration and how we solved Kepler's equation are reported in Appendix A. The solution of the previous equations of motion gives the spherical coordinates of the star in the BH reference frame, related with Cartesian coordinates $\{x_{\text{BH}}, y_{\text{BH}}, z_{\text{BH}}\}$ via the usual transformation. In this frame, z_{BH} is aligned with the BH spin axis. Following Grould et al. (2017), we can define a new reference frame $\{x', y', z_{\text{obs}}\}$ such that $x' = \text{DEC}$, $y' = \text{R.A.}$ are the collected astrometric data, z_{obs} points towards the BH and $v_{z_{\text{obs}}}$ corresponds to the radial velocity. Despite most of the S2 motion occurring in a Newtonian regime (i.e. with $v \ll 1$) making the above classical approximation appropriate, near the periastron it reaches a total space velocity of $v \approx 7650\,\text{km s}^{-1} \sim 10^{-2}$. In this region, the numerical solution $v_{z_{\text{obs}}}$ obtained from equations (15) must be corrected. We include the two main relativistic effects in order to model the measured radial velocity V_{R}: the relativistic Doppler shift and the gravitational redshift. Moreover, due to the finite speed of light propagation, the dates of observation t_{obs} are generally different from the dates of emission t_{em}. This is a pure classical effect known as Rømer's delay and for S2, we have $\Delta t = t_{\text{em}} - t_{\text{obs}} \approx 8\,\text{d}$ on average over the entire orbit. Including this effect in our simulation requires solving the so-called Rømer's equation, namely:

$$t_{\text{obs}} - t_{\text{em}} - z_{\text{obs}}(t_{\text{em}}) = 0 \qquad (19)$$

(here we corrected a minus sign in Grould et al. (2017)) that we solved using its first-order Taylor's expansion, as already done in GRAVITY Collaboration (2018a); Heißel et al. (2022).

Details about how to implement the transformation between the orbital frame and the observer frame, how to include the relativistic corrections and how we solved equation (19) are reported in Appendix B.

2.3 Data

The set of available data D can be divided as follows:

a) Astrometric data DEC, R.A.

    (a) 128 data points collected using both the SHARP camera at New Technology Telescope (TNN) between 1992 and 2002 ($\sim$10 data points, accuracy $\approx$4 mas) and the NACO imager at the VLT between 2002 and 2019 (118 data points, accuracy $\approx$0.5 mas);

    (b) 76 data points collected by GRAVITY at VLT between 2016 and April 2022 (accuracy $\approx$50 μas).

b) Spectroscopic data V_{R}

    (a) 102 data points collected by SINFONI at the VLT (100 points) and NIRC2 at Keck (2 points) collected be-

Table 1. Uniform priors used in the MCMC analysis. Initial guesses Θ_i^0 coincide with the best-fit parameters found by **minimize**.

Parameter	Θ_i^0	Lower bound	Upper bound
e	0.88441	0.83	0.93
a_{sma} [as]	0.12497	0.119	0.132
i_{orb} [°]	134.69241	100	150
ω_{orb} [°]	66.28411	40	90
Ω_{orb} [°]	228.19245	200	250
t_{p} [yr]	2018.37902	2018	2019
M [$10^6\,\text{M}_\odot$]	4.29950	4.1	4.8
R_0 [10^3 pc]	8.27795	8.1	8.9
Λ	0.001	0	1

tween 2000 and March 2022 (accuracy in good conditions $\approx$10–15 km s^{-1}).

2.4 Model fitting approach

To fit S2 data, we perform a Markov Chain Monte Carlo (MCMC) analysis using the Python package EMCEE (Foreman-Mackey et al. 2013). The fitting procedure is as follows: we set the value of the mass coupling α roughly within the range reported in (12). For any given value of α, we fit for the following set of parameters,

$$\Theta_i = \{e, a_{\text{sma}}, \Omega_{\text{orb}}, i_{\text{orb}}, \omega_{\text{orb}}, t_{\text{p}}, R_0, M, x_0, y_0, v_{x_0}, v_{y_0}, v_{z_0}, \Lambda\},$$
$$(20)$$

where Ω_{orb}, i_{orb}, and ω_{orb} are the three angles used to project the orbital frame in the observer reference frame using the procedure reported in Appendix B1. The additional parameters $\{x_0, y_0, v_{x_0}, v_{y_0}, v_{z_0}\}$ characterize the NACO/SINFONI data reference frame with respect to Sgr A* (Plewa et al. 2015). The log-likelihood is given by

$$\ln \mathcal{L} = \ln \mathcal{L}_{\text{pos}} + \ln \mathcal{L}_{\text{vel}}, \qquad (21)$$

where

$$\ln \mathcal{L}_{\text{pos}} = -\sum_{i=1}^{N}\left[\frac{(\text{DEC}_i - \text{DEC}_{\text{model},i})^2}{\sigma_{\text{DEC}_i}^2} + \frac{(\text{R.A.}_i - \text{R.A.}_{\text{model},i})^2}{\sigma_{\text{R.A.},i}^2}\right], \qquad (22)$$

and

$$\ln \mathcal{L}_{\text{vel}} = -\sum_{i=1}^{N} \frac{(V_{\text{R},i} V_{\text{model},i})^2}{\sigma_{V_{\text{R},i}}^2}. \qquad (23)$$

The priors we used are listed in Table 1. We used uniform priors for the physical parameters, i.e. we only imposed physically motivated bounds and Gaussian priors for the additional parameters describing NACO data, since the latter have been instead well constrained by previous work by Plewa et al. (2015) and are not expected to change.

The initial points Θ_i^0 in the MCMC are chosen such that they minimize the χ^2 when $f_{\text{SP}} = 1$ and $\Lambda = 0$. The minimization is performed using the Python package **lmfit.minimize** (Newville et al. 2016) with Levenberg–Marquardt method. In the sampling phase of the MCMC implementation, we used 64 walkers and 10^5 iterations. Since we started our MCMC at the minimum found by **minimize,** we skipped the burning-in phase and we used the last 80 per cent of the chains to compute the mean and standard deviation of the posterior distributions. The convergence of the MCMC analysis is assured by means of the autocorrelation time τ_{c}, i.e. we ran N iterations such that $N \gg 50\tau_{\text{c}}$.

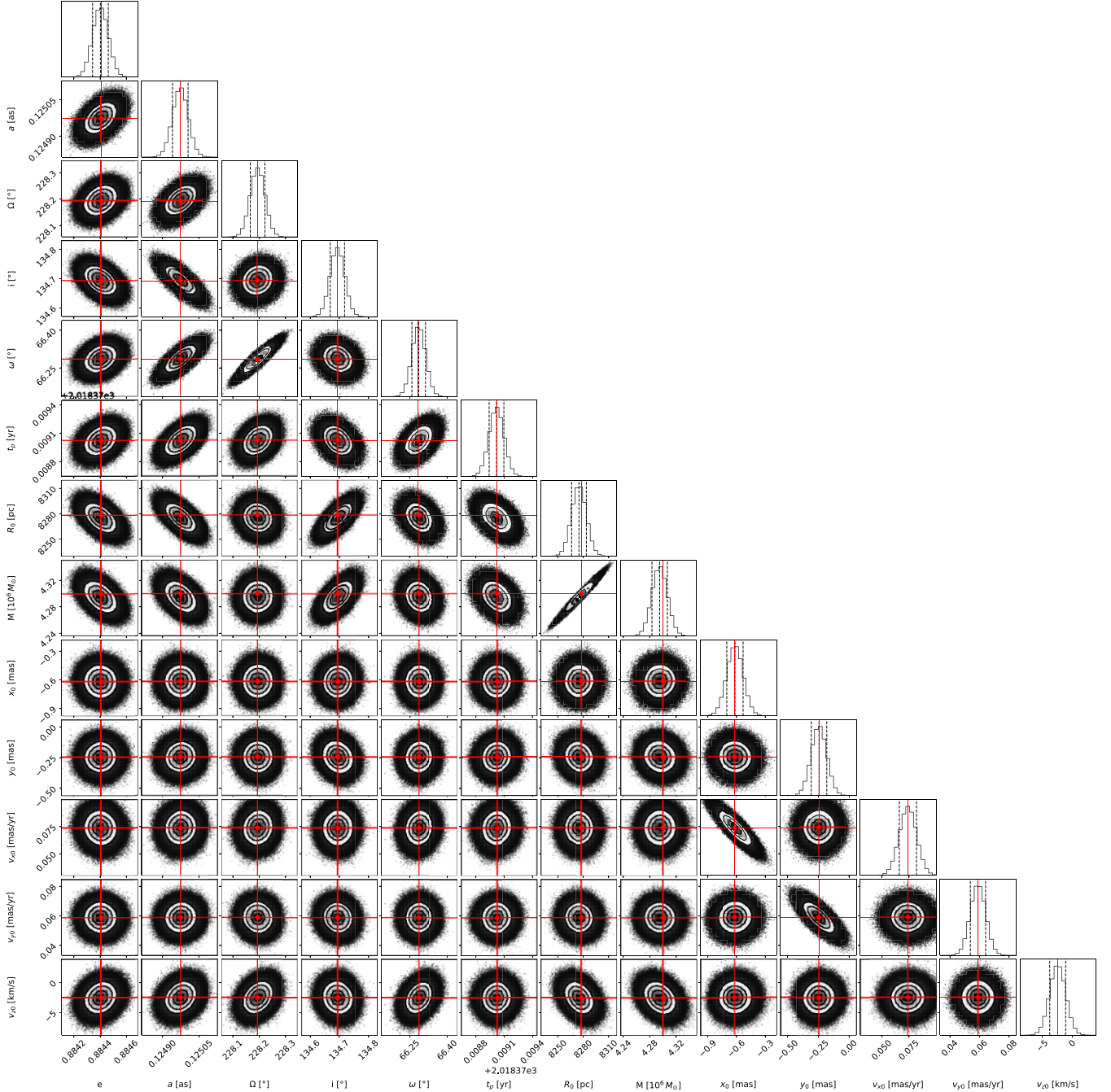**Figure 2.** Corner plot of the fitted parameters with $f_{SP} = 1$ and $\Lambda = 0$. Red lines represent values from **minimize**, while dashed black lines represent the mean value and 1σ interval of the posterior distributions.

In a first preliminary check we set $\Lambda = 0$ and we fit for the first 13 parameters of (20) imposing $f_{SP} = 1$. In Fig. 2, we report the corner plot of the parameters, which are in very good agreement with the previous best estimates obtained in GRAVITY Collaboration (2022). In the following, we assume that z_{BH} is aligned with z_{orb}, i.e. the direction of the BH spin axis is aligned with the angular momentum of the S2 orbit. This means that the motion happens in the equatorial plane ($\theta = \pi/2$) of the BH and the initial conditions for the numerical integration of the orbit are those reported in (18). We fit for the 14 parameters listed in (20).

3 RESULTS

Before running the MCMC algorithm, we used a χ^2 minimiser to evaluate the best-fit values of Λ and to quantify how accurately we can constrain the scalar cloud mass. Results are summarised in Fig. 3. For very small ($\alpha \lesssim 0.0035$) or large ($\alpha \gtrsim 0.045$) values of α, Λ has very large uncertainties, and the results are compatible with $\Lambda = 0$, i.e. having a vacuum environment.

Uncertainties on Λ become much smaller in the range $0.01 \lesssim \alpha \lesssim 0.03$. The underlying reason for this can be understood from the
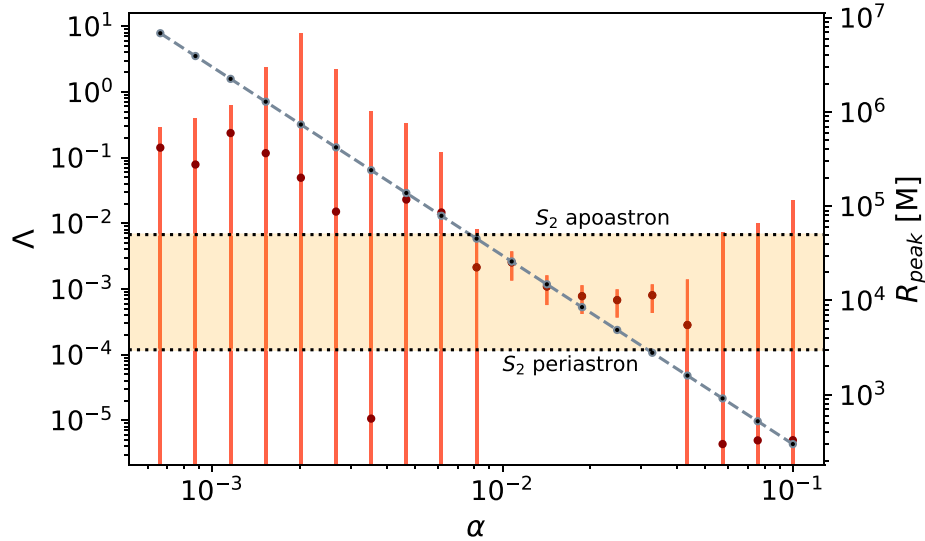
Figure 3. Best fit values of Λ with 1σ uncertainty when α is fixed and it is varied over the range $[6 \cdot 10^{-4}, 10^{-1}]$. The dashed grey line represents R_{peak} as a function of α as illustrated in (24). The yellow band represents the orbital range of S2 delimited by its apoastron and periastron positions. Although a nonzero value of Λ is apparent for a restricted range of α, the statistical significance of this finding is not significant, see Table 3.

effective peak position of the scalar density distribution

$$R_{\text{peak}} = \frac{\int_0^\infty \rho \bar{r} \, d\bar{r}}{\int_0^\infty \rho \, d\bar{r}} = \frac{3M}{\alpha^2}. \qquad (24)$$

For the range of α above, one finds $3000M \lesssim R_{\text{peak}} \lesssim 30\,000\,M$, i.e. when R_{peak} is located between S2's apoastron and periastron and the star crosses regions of higher density. This analysis is reported in Fig. 3, where we show the behaviour of R_{peak} as a function of α, dictated by equation (24), and S2's apoastron and periastron.

Notice that Fig. 3 seems to indicate that the motion of S2 is compatible with a cloud of scalar field for $0.01 < \alpha < 0.03$. However, as we now discuss, the statistical evidence for a nonzero Λ is not significant.

MCMC results confirm the trend observed in Fig. 3 but provide more insight into how Λ is distributed in the range of α considered. In particular, we looked for the maximum likelihood estimator (MLE) of Λ, i.e. $\hat{\Lambda} = \arg\max \mathcal{L}(\Lambda; D)$. Results are summarized in Fig. 4. For $0.006 < \alpha < 0.075$, the posteriors $P(\Lambda_\alpha|D)$ look like normal distributions. Here, $\hat{\Lambda}$ and associated uncertainties coincide with the mean and standard deviation of the distributions, and they are roughly the same reported in Fig. 3. However, when we move away from this range, the posteriors start to be peaked around zero and $\hat{\Lambda}$ does not coincide with the mean value of the distributions anymore, as a result of the prior bounds we imposed on Λ. Since in these cases $\hat{\Lambda}$ is always very close to zero (and far below the precision of current instruments), we estimated Λ_1 and Λ_2 such that $P(\Lambda_\alpha < \Lambda_1|D) \approx 68$ per cent and $P(\Lambda_\alpha < \Lambda_2|D) \approx 99$ per cent of $P(\Lambda_\alpha|D)$. In this way, we were able to obtain a rough upper bound on the fractional mass at 1, 3σ confidence levels, reported in parenthesis in Table 3. We notice also that for smaller values of α, $P(\Lambda_\alpha|D)$ flattens out, showing the difficulties of finding a meaningful MLE $\hat{\Lambda}$ as soon as the cloud is located far away from S2's apoastron. These features are shown in Fig. 4, where we report the one-dimensional projection of the (marginalised) posterior distributions of Λ for the values of α reported in Table 3. We also show the mean (red-dashed line) when distributions are normal and the 1σ confidence interval (orange band, evaluated as explained above when the distribution is non-normal). Not surprisingly, we noticed that basically no relevant information

can be extracted from those confidence intervals when R_{peak} is far from S2's apoastron. However, in the case with $\alpha = 0.075$, which corresponds to $R_{\text{peak}} \approx 530\,M$, we found that $\Lambda \lesssim 5 \cdot 10^{-3}$ at $3\,\sigma$ confidence level, roughly recovering the upper bound $\delta M \lesssim 10^{-3}\,M$ found in GRAVITY Collaboration (2022).

In order to determine the statistical significance of our results we computed the Bayes factor K, i.e. the ratio of the maximum likelihood computed for different values of α and $\hat{\Lambda}$ reported in Table 3 (that we call model α) to the maximum likelihood associated with the non-perturbative case (model 0). According to Kass & Raftery (1995) if $1 \leq \log_{10} K \leq 2$, there is a strong evidence that model α is preferred over model 0, while if $\log_{10} K > 2$, the strength of evidence is decisive. Negative values of $\log_{10} K$ correspond to negative evidence, i.e. model 0 is preferred over model α. As expected, we found $\log_{10} K \ll 1$, every time the cloud is located far away from S2 orbital range. In contrast, when $r_{\text{apo, S2}} \lesssim R_{\text{peak}} \lesssim r_{\text{peri, S2}}$, there is only mild evidence that model α is preferred over model 0 (we found $\log_{10} K < 2$ always).

4 DISCUSSION

Precision observations by the GRAVITY instrument can now be used to set exquisite constraints on possible dark matter structures around Sgr A*. We have shown that with current observations, scalar clouds – possibly of superradiant origin, with mass couplings in the range $\alpha \in [0.015, 0.045]$ can be ruled out, for cloud masses $\Lambda \gtrsim 0.1\%$ of the central BH mass (equivalent to $\delta M \sim 4000\,M_\odot$). It is similar to that of GRAVITY Collaboration (2022), who provided a 1σ upper bound of 0.1% of M on the observational dark mass within the orbit of S2 assuming a Plummer profile for the distribution.

We also note that, for certain scalar couplings α, observational data are well fitted by a non-zero value of Λ of order 10^{-3}. However, all these values of Λ are consistent with zero within the 3σ confidence interval. The computation of the Bayes' factor showed that this perturbed model is only mildly preferred over the non-perturbed model predicting a single central BH without a cloud. We conclude that there is no strong evidence to claim the existence of a scalar cloud around Sgr A* described by our set-up.
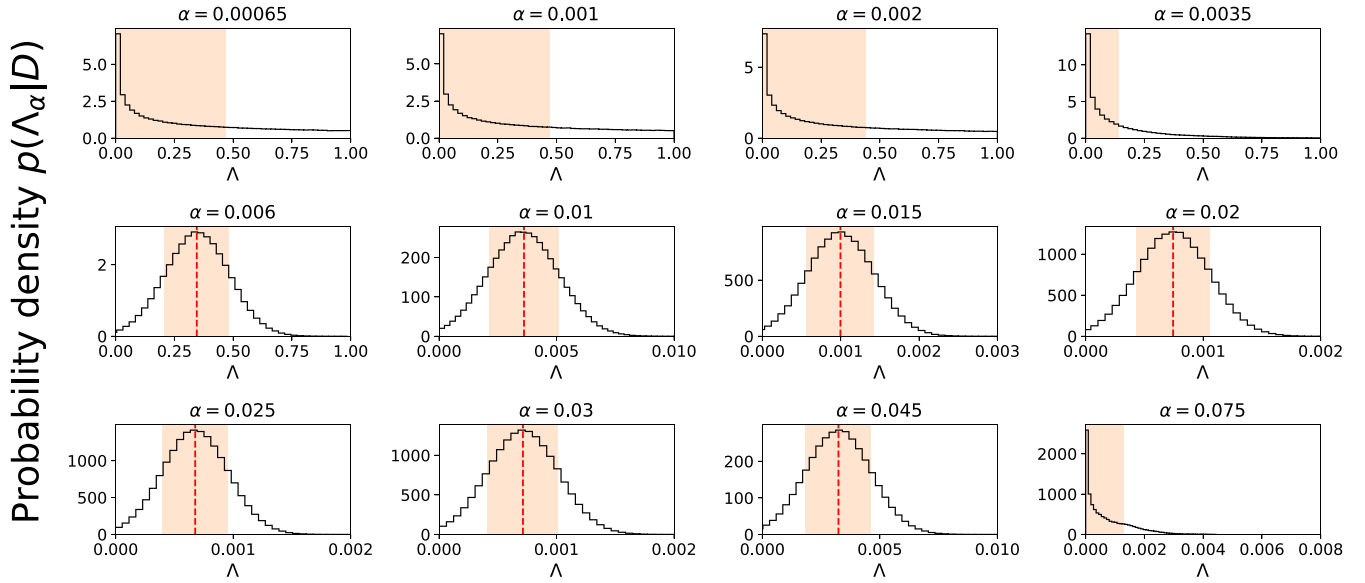
Figure 4. Posterior probability densities $P(\Lambda_\alpha|D)$ for different values of α. Red-dashed lines represent the mean value of Gaussian distributions (which coincides with the MLE $\hat{\Lambda}$), while orange bands correspond to 1σ confidence level, i.e. $\approx 68\%$ of $P(\Lambda_\alpha|D)$ lies in that region.

Table 2. Gaussian priors used in the MCMC analysis. Initial guesses Θ_i^0 coincide with the best-fit parameters found by **minimize**. ξ and σ represent the mean and the standard deviation of the distributions, respectively, and they come from Plewa et al. (2015).

Parameter	Θ_i^0	ξ	σ
x_0 [mas]	-0.244	-0.055	0.25
y_0 [mas]	-0.618	-0.570	0.15
v_{x_0} [mas yr^{-1}]	0.059	0.063	0.0066
v_{y_0} [mas yr^{-1}]	0.074	0.032	0.019
v_{z_0} [km s^{-1}]	-2.455	0	5

Table 3. Maximum Likelihood Estimator $\hat{\Lambda}$ with associated 1σ error and Bayes factors $\log_{10} K$ for different values of α. The measurements for each α are not independent (the same orbit was used to derive them) and therefore cannot be combined to derive a more stringent upper limit. For non-normal distributions we report Λ_1 and Λ_2 defined such that $P(\Lambda_\alpha < \Lambda_1|D) \approx 68\%$ and $P(\Lambda_\alpha < \Lambda_2|D) \approx 99\%$ of $P(\Lambda_\alpha|D)$.

α	$\hat{\Lambda}$	$\log_{10} K$
0.00065	$\lesssim (0.470, 0.980)$	0.09
0.001	$\lesssim (0.470, 0.980)$	0.08
0.002	$\lesssim (0.440, 0.978)$	-0.06
0.0035	$\lesssim (0.140, 0.780)$	-10.58
0.006	0.34671 ± 0.13666	1.44
0.01	0.00361 ± 0.00147	1.29
0.015	0.00101 ± 0.00042	1.24
0.02	0.00075 ± 0.00030	1.33
0.025	0.00068 ± 0.00028	1.35
0.03	0.00073 ± 0.00029	1.33
0.045	0.00328 ± 0.00135	1.27
0.075	$\lesssim (0.0013, 0.0052)$	0.0001

Stronger constraints, or a detection, require more observations or the inclusion of other stars of the S-cluster in the fit. However, since the potential describing the cloud is non-spherically symmetric, the inclination of stars with each other plays a fundamental role,

at least in theory, and this same analysis can not be performed straightforwardly. For the same reason, we were forced to set an initial angular position for S2 co-planar with the BH equator ($\theta = \pi/2$). This is the simplest choice but also the one that maximizes the scalar potential in equation (9), i.e. our chances to actually detect the cloud. We can try to quantify the error we are making in setting the initial angular position of the star, by looking at the difference in the orbits for two different initial inclinations: $\theta = \pi/2$ and $\theta = 0$, focusing on the interesting range of α: $0.01 \leq \alpha \leq 0.045$. We found that the maximum relative (per centage) difference in the astrometry is achieved for $\alpha = 0.01$, where $\Delta\text{DEC} \sim \Delta\text{R.A.} \approx 25\%$, while the maximum difference in the radial velocity is found to be $\Delta V_R \approx 15\%$ for $\alpha = 0.045$. Although these differences may seem significant, we point out that: (i) they would be smaller for any values of $\theta \in [0, \pi/2]$ and (ii) they are only reached in correspondence of the two periastron passages, while they remain much smaller over the rest of the orbit. Hence, we are relatively confident that there will be no significant changes in the best-fit parameters we found for different initial inclinations of S2. In addition, GRAVITY Collaboration (2019a) showed that also the inclination of Sgr A*'s spin with respect to the observer frame plays an important role in the effects the cloud has on S2 motion. Indeed, results including the motion of other S-stars and Sgr A*'s spin direction are left for future works.

Recently, Sengo et al. (2023) studied constraints on scalar structures using EHT data. Not surprisingly, bounds are of order $\Lambda \sim 10\%$, compatible with the measurement precision of the telescope. Our results improve consistently and considerably this estimate for Sgr A*, showing that a bosonic structure can only exist with a maximum (fractional) mass of $\Lambda \approx 10^{-3}$, at least for spin 0 fields.

Yuan et al. (2022) used the motion of S2 to derive an upper limit of $\delta M \lesssim 10^{-4} M$ for a scalar cloud with particle mass $m_s = 10^{-18}$ eV ($\alpha \sim 0.015$) interacting with either the Higgs boson or the photon. Their estimate only uses publicly available and not GRAVITY data, which, due to their very small uncertainties, dominate our likelihood. This is reflected in the best-fit parameters found, which are not compatible (within 3σ uncertainties) with the most recent ones reported in GRAVITY Collaboration (2022). We argue that

this difference already at the non-perturbative level may lead to misleading results when the cloud is included in the fit.

Finally, we point out that the spin of Sgr A* is relevant when discussing superradiant phenomena, since it affects the possible origin of the scalar cloud. Despite recent work by Fragione & Loeb (2020) placing a strong constraint on Sgr A* spin parameter ($\chi \lesssim 0.1$), other studies (Qi 2021, O'Shaughnessy & Brady 2021) question such a result and show that the current astrometric measurements are not yet sufficient to constrain the value of the spin. On the other hand, Kato et al. (2010) used quasi-periodic oscillations in the radio emissions of Sgr A* to claim that its spin is $\chi = 0.44 \pm 0.08$. The current best estimate for Sgr A*'s spin comes from the EHT observations (Broderick et al. 2011), which reported a measurement of $\chi = 0.00 \pm 0.64$, where the error is the 1σ uncertainty. Due to the high uncertainty of these results and the ongoing discussion about it, it can be assumed without loss of generality that Sgr A* is (was) in fact spinning enough to engage a superradiant instability. We note, however, that even a non-spinning BH can bind a scalar 'cloud' if it was grown via some other mechanism (for example, primordial, Cardoso et al. (2022a)).

An upgrade of the Gravity experiment towards Gravity+ is ongoing at the time of writing, as well as the commissioning of the ERIS instrument. The increased sensitivity of Gravity + and the patrol field of view of ERIS strongly increase the prospects of detecting and tracking further stars in inner orbits, putting stronger constraints on the scalar cloud.

DATA AVAILABILITY

Publicly available data for astrometry and radial velocity up to 2016.38 can be found in Table 5 the electronic version of Gillessen et al. (2017) at this link: https://iopscience.iop.org/article/10.3847/1538-4357/aa5c41/meta#apjaa5c41t5.

REFERENCES

Abbott L. F., Sikivie P., 1983, Phys. Lett. B, 120, 133

Akiyama K., et al., 2022, Astrophys. J. Lett., 930, L12

Arvanitaki A., Dimopoulos S., Dubovsky S., Kaloper N., March-Russell J., 2010, Phys. Rev. D, 81, 123530

Bar N., Blum K., Lacroix T., Panci P., 2019, JCAP, 2019, 045

Bertone G., Merritt D., 2005, Phys. Rev. D, 72, 103502

Brito R., Cardoso V., Pani P., 2015a, Class. Quant. Grav., 32, 134001

Brito R., Cardoso V., Pani P., 2015b, Lect. Notes Phys., 906, 1

Broderick A. E., Fish V. L., Doeleman S. S., Loeb A., 2011, Astrophys. J., 735, 110

Cardoso V., Chakrabarti S., Pani P., Berti E., Gualtieri L., 2011, Phys. Rev. Lett., 107, 241101

Cardoso V., Ikeda T., Vicente R., Zilhão M., 2022b, Phys. Rev. D, 106, L121302

Cardoso V., Ikeda T., Zhong Z., Zilhão M., 2022a, Phys. Rev. D, 106, 044030

Cardoso V., Yoshida S., 2005, JHEP, 2005, 009

Catanzarite J. H., 2010, preprint (arXiv:1008.3416)

de Laurentis M., de Martino I., Della Monica R., 2022, The Galactic Center as a laboratory for theories of gravity and dark matter, preprint (arXiv:2211.07008)

Della Monica R., de Martino I., 2023, Astronomy&Astrophysics, 670, L4

Detweiler S. L., 1980, Phys. Rev. D, 22, 2323

Dine M., Fischler W., 1983, Phys. Lett. B, 120, 137

Dolan S. R., 2007, Phys. Rev. D, 76, 084001

Eckart A., Genzel R., 1996, Nature, 383, 415

Ferreira M. C., Macedo C. F. B., Cardoso V., 2017, Phys. Rev. D, 96, 083017

Foreman-Mackey D., Hogg D. W., Lang D., Goodman J., 2013, PASP, 125, 306

Fragione G., Loeb A., 2020, Astrophys. J. Lett., 901, L32

Fujita R., Cardoso V., 2017, Phys. Rev. D, 95, 044016

Genzel R., Eisenhauer F., Gillessen S., 2010, Rev. Mod. Phys., 82, 3121

Ghez A. M. et al., 2003, ApJ, 586, L127

Ghez A. M. et al., 2008, ApJ, 689, 1044

Gillessen S. et al., 2017, ApJ, 837, 30

Gillessen S., Eisenhauer F., Fritz T. K., Bartko H., Dodds-Eden K., Pfuhl O., Ott T., Genzel R., 2009b, ApJ, 707, L114

Gillessen S., Eisenhauer F., Trippe S., Alexander T., Genzel R., Martins F., Ott T., 2009a, ApJ, 692, 1075

Gondolo P., Silk J., 1999, Phys. Rev. Lett., 83, 1719

GRAVITY Collaboration, 2017, A&A, 602, A94

GRAVITY Collaboration, 2018a, A&A, 615, L15

GRAVITY Collaboration, 2018b, A&A, 618, L10

GRAVITY Collaboration, 2019a, MNRAS, 489, 4606

GRAVITY Collaboration, 2019b, A&A, 625, L10

GRAVITY Collaboration, 2020, A&A, 636, L5

GRAVITY Collaboration, 2022, A&A, 657, L12

Grould M., Vincent F. H., Paumard T., Perrin G., 2017, A&A, 608, A60

Habibi M. et al., 2017, ApJ, 847, 120

Heißel G., Paumard T., Perrin G., Vincent F., 2022, A&A, 660, A13

Kass R. E., Raftery A. E., 1995, J. Am. Statist. Assoc., 90, 773

Kato Y., Miyoshi M., Takahashi R., Negoro H., Matsumoto R., 2010, MNRAS, 403, 74

Kodama H., Yoshino H., 2012, Int. J. Mod. Phys. Conf. Ser., 07, 84

Lacroix T., 2018, Astron. Astrophys., 619, A46

Merritt D., 2004, Phys. Rev. Lett., 92, 201304

Merritt D., Milosavljevic M., Verde L., Jimenez R., 2002, Phys. Rev. Lett., 88, 191301

Newville M., Stensitzki T., Allen D. B., Rawlik M., Ingargiola A., Nelson A., 2016, Lmfit: Non-Linear Least-Square Minimization and Curve-Fitting for Python, Astrophysics Source Code Library, record(ascl:1606.014)

Peccei R. D., Quinn H. R., 1977, Phys. Rev. Lett., 38, 1440

Plewa P. M. et al., 2015, MNRAS, 453, 3234

Poisson E., Will C., 2014, Gravity: Newtonian, Post-Newtonian, Relativistic. Cambrigde University Press, Cambridge

Preskill J., Wise M. B., Wilczek F., 1983, Phys. Lett. B, 120, 127

Qi H., O'Shaughnessy R., Brady P., 2021, Phys. Rev. D, 103, 084006

Reid M. J., Brunthaler A., 2020, ApJ, 892, 39

Sabha N., et al., 2012, A&A, 545, A70

Sadeghian L., Ferrer F., Will C. M., 2013, Phys. Rev. D, 88, 063522

Schödel R. et al., 2002, Nature, 419, 694

Sengo I., Cunha P. V. P., Herdeiro C. A. R., Radu E., 2023, JCAP, 2023, 047

Weinberg S., 1978, Phys. Rev. Lett., 40, 223

Wilczek F., 1978, Phys. Rev. Lett., 40, 279

Will C. M., 2008, Astrophys. J. Lett., 674, L25

Witek H., Cardoso V., Ishibashi A., Sperhake U., 2013, Phys. Rev. D, 87, 043513

Yuan G.-W., Shen Z.-Q., Tsai Y.-L. S., Yuan Q., Fan Y.-Z., 2022, Phys. Rev. D, 106, 103024

Zhao H., 1996, MNRAS, 278, 488

APPENDIX A: DETAILS ABOUT NUMERICAL INTEGRATION

The numerical integration of the equation of motion in (15) is performed making use of the PYTHON library **scipy.integrate.solve_ivp** with a Runge–Kutta 5(4) algorithm, meaning that the steps are evaluated using a 5-th order method while the error is controlled assuming the accuracy of the 4-th order method. The convergence of the integration is assured by looking at the conservation of energy over the entire integration period (almost two orbits in ~ 30 years gives $\Delta E/E \sim \mathcal{O}(10^{-10})$).

Kepler's equation is solved instead using a PYTHON's root finder (**scipy.optimize.newton**), which implements a Newton–Raphson method. The latter solves the equation with precision of $\mathcal{O}(10^{-16})$.

APPENDIX B: COORDINATES TRANSFORMATIONS AND INCLUSION OF RELATIVISTIC EFFECTS

B1 Coordinate transformation

The transformation from the orbital reference frame to the observer reference frame can be achieved using the following conversion:

$$
\begin{aligned}
x' &= A x_{\text{BH}} + F y_{\text{BH}} & v_{x'} &= A v_{x_{\text{BH}}} + F v_{y_{\text{BH}}} \\
y' &= B x_{\text{BH}} + G y_{\text{BH}} & v_{y'} &= B v_{x_{\text{BH}}} + G v_{y_{\text{BH}}} \\
z_{\text{obs}} &= -(C x_{\text{BH}} + H y_{\text{BH}}) & v_{z_{\text{obs}}} &= -(C v_{x_{\text{BH}}} + H v_{y_{\text{BH}}}),
\end{aligned}
\tag{B1}
$$

where A, B, C, F, G, H are the Thiele-Innes parameters (Catanzarite 2010) defined as:

$$
\begin{aligned}
A &= \cos \Omega \cos \omega - \sin \Omega \sin \omega \cos i \\
B &= \sin \Omega \cos \omega + \cos \Omega \sin \omega \cos i \\
F &= -\cos \Omega \sin \omega - \sin \Omega \cos \omega \cos i \\
G &= -\sin \Omega \sin \omega + \cos \Omega \cos \omega \cos i \\
C &= -\sin \omega \sin i \\
H &= -\cos \omega \sin i,
\end{aligned}
\tag{B2}
$$

while the Cartesian coordinates $\{x_{\text{BH}}, y_{\text{BH}}, z_{\text{BH}}\}$ and velocities $\{v_{x_{\text{BH}}}, v_{y_{\text{BH}}}, v_{z_{\text{BH}}}\}$ are those obtained from the numerical integration. For a more detailed discussion about how the coordinate system $\{x', y', z_{\text{obs}}\}$ and the above transformation are defined we refer the reader to Fig. 1 and Appendix B of Grould et al. (2017).

B2 Relativistic effects and Rømer's delay

As said in the main text, there are two main contributions that must be taken in consideration when S2 approaches the periastron: the relativistic Doppler shift and the gravitational redshift. Both of them induce a shift in the spectral lines of S2 that affects the radial velocity measurments. The former is given by

$$
1 + z_{\text{D}} = \frac{1 + v_{z_{\text{obs}}}}{\sqrt{1 - v^2}},
\tag{B3}
$$

while the gravitational redshift is defined as

$$
1 + z_{\text{G}} = \frac{1}{\sqrt{1 - 2M/r_{\text{em}}}}.
\tag{B4}
$$

The two shifts can be combined using Eq.(D.13) of Grould et al. (2017) to obtain the total radial velocity

$$
V_{\text{R}} \approx \frac{1}{\sqrt{1 - \epsilon}} \cdot \frac{1 + v_{z_{\text{obs}}}/\sqrt{1 - \epsilon}}{\sqrt{1 - v^2/(1 - \epsilon)}} - 1.
\tag{B5}
$$

where $\epsilon = 2M/r_{\rm em}$. In the total space velocity $v = |\mathbf{v}|$, we must also add a correction due to the Solar system motion. We followed the most recent work of Reid & Brunthaler (2020) and take a proper motion of Sgr A∗ of

$$v_x^{\rm SSM} = -5.585\,{\rm mas\,yr^{-1}} = 6.415\cos(209.47°)\,{\rm mas\,yr^{-1}},$$
$$v_y^{\rm SSM} = -3.156\,{\rm mas\,yr^{-1}} = 6.415\sin(209.47°)\,{\rm mas\,yr^{-1}}. \quad (B6)$$

The Rømer's delay is instead included using the first order Taylor's expansion of equation (19), which reads:

$$t_{\rm em} = t_{\rm obs} - \frac{z_{\rm obs}(t_{\rm obs})}{1 + v_{z_{\rm obs}}(t_{\rm obs})}. \quad (B7)$$

The difference between the exact solution of equation (19) and the approximated one in (B7) is at most ∼4 s over S2 orbit and therefore negligible. The Rømer effect affects both the astrometry and the spectroscopy, with an impact of ≈450 μas on the position and ≈50 km s⁻¹ at periastron for the radial velocity. Our results recover the previous estimates for this effect in Grould et al. (2017); GRAVITY Collaboration (2018a).

APPENDIX C: CORNER PLOTS

Here, we report the corner plots for two representative values of α ($\alpha = 0.01$ and $\alpha = 0.001$), to show the behaviour of the parameters when the cloud is located inside and outside S2's orbital range. The strong correlation between Λ and the periastron passage $t_{\rm p}$ when $\alpha = 0.01$ can be understood following the argument of Heißel et al. (2022): the presence of an extended mass will induce a retrograde precession in the orbit that will result in a positive shift of the periastron passage time, needed to compensate the (negative) shift in the initial true anomaly. Indeed, when considering the Schwarzschild precession, which instead induces a prograde precession (hence a positive initial shift in the true anomaly), $t_{\rm p}$ will undergo a negative shift, as can be seen from the strong anticorrelation between $f_{\rm SP}$ and $t_{\rm p}$ reported in GRAVITY Collaboration (2020).

[1]CENTRA - Centro de Astrofísica e Gravitação, IST, Universidade de Lisboa, 1049-001 Lisboa, Portugal
[2]Faculdade de Engenharia, Universidade do Porto, rua Dr Roberto Frias, 4200-465 Porto, Portugal
[3]European Southern Observatory, Karl-Schwarzschild-Straße 2, D-85748 Garching, Germany
[4]LESIA, Observatoire de Paris, Université PSL, CNRS, Sorbonne Université, Université de Paris, 5 place Jules Janssen, F-92195 Meudon, France
[5]Universitat Politècnica de València, València, Spain
[6]Max Planck Institute for extraterrestrial Physics, Giessenbachstraße 1, D-85748 Garching, Germany
[7]Kavli Institute for Astronomy and Astrophysics, Beijing, China
[8]Higgs Centre for Theoretical Physics, Edinburgh, UK
[9]Universidade de Lisboa - Faculdade de Ciências, Campo Grande, 1749-016 Lisboa, Portugal
[10]Department of Physics, University of Illinois, 1110 West Green Street, Urbana, IL 61801, USA
[11]Univ. Grenoble Alpes, CNRS, IPAG, F-38000 Grenoble, France
[12]Max Planck Institute for Astronomy, Königstuhl 17, D-69117 Heidelberg, Germany
[13]Niels Bohr International Academy, Niels Bohr Institute, Blegdamsvej 17, DK-2100 Copenhagen, Denmark
[14]Leiden University, 2311EZ Leiden, The Netherlands
[15]Institute of Astronomy, KU Leuven, Celestijnenlaan 200D, B-3001 Leuven, Belgium
[16]Department of Astrophysical & Planetary Sciences, JILA, Duane Physics Bldg., 2000 Colorado Ave, University of Colorado, Boulder, CO 80309, USA
[17]1st Institute of Physics, University of Cologne, Zülpicher Straße 77, D-50937 Cologne, Germany
[18]Max Planck Institute for Radio Astronomy, auf dem Hügel 69, D-53121 Bonn, Germany
[19]Hamburger Sternwarte, Universität Hamburg, Gojenbergsweg 112, D-21029 Hamburg, Germany
[20]Departments of Physics and Astronomy, Le Conte Hall, University of California, Berkeley, CA 94720, USA
[21]European Southern Observatory, Casilla 19001, Santiago 19, Chile
[22]Advanced Concepts Team, European Space Agency, TEC-SF, ES-TEC, Keplerlaan 1, NL-2201, AZ Noordwijk, The Netherlands
[23]School of Physics & Astronomy, University of Southampton, Southampton, SO18 4EX, United Kingdom
[24]Université Côte d'Azur, Observatoire de la Côte d'Azur, CNRS, Lagrange, France
[25]Max Planck Institute for Astrophysics, Karl-Schwarzschild-Straße 1, D-85748 Garching, Germany
[26]ORIGINS Excellence Cluster, Boltzmannstraße 2, D-85748 Garching, Germany

This paper has been typeset from a TEX/LATEX file prepared by the author.

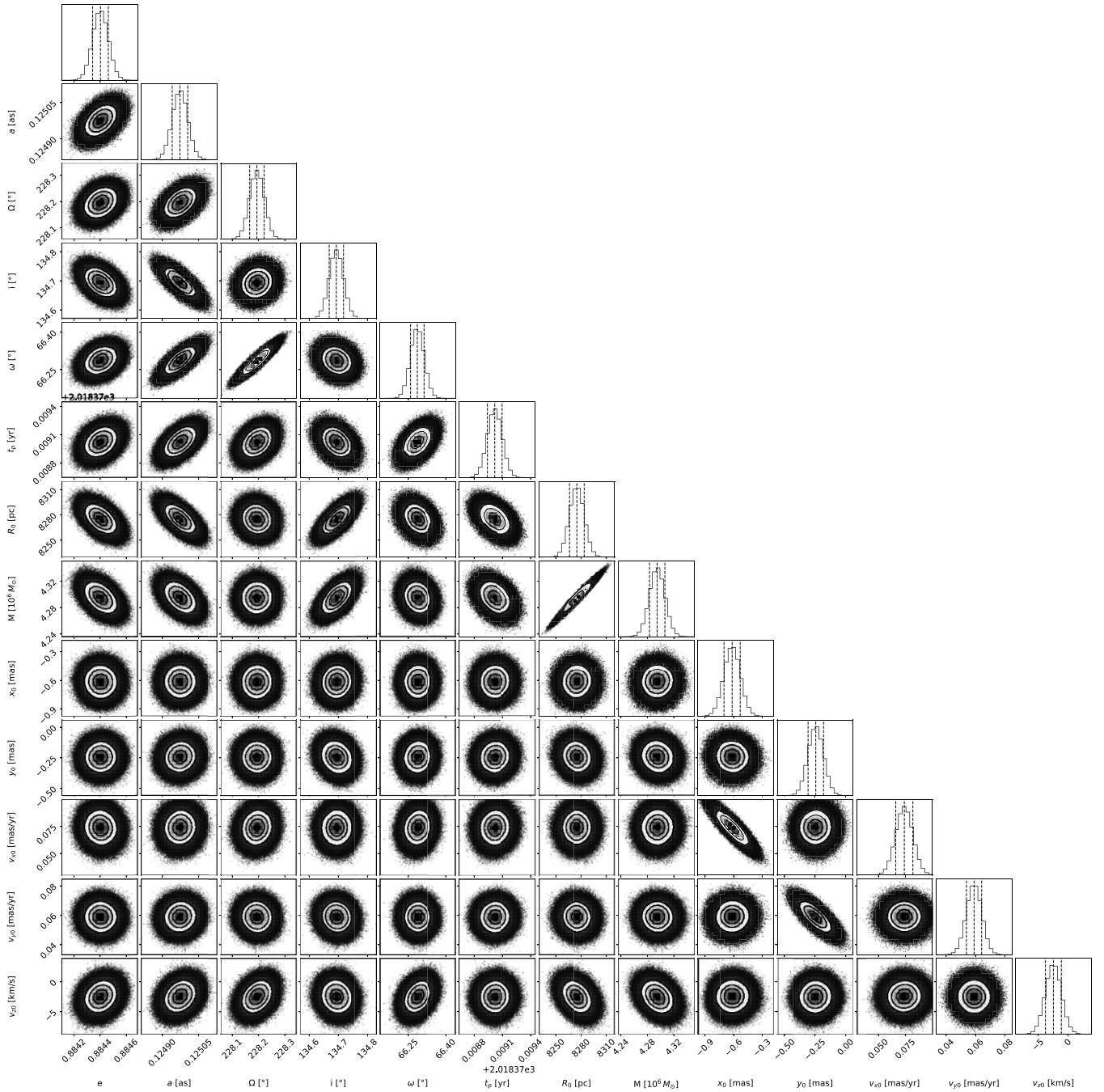**Figure C1.** Corner plot of the fitted parameters with $f_{SP} = 1$ and $\alpha = 0.01$. Dashed lines represent the 0.16, 0.50, and 0.84 quantiles of the distributions.
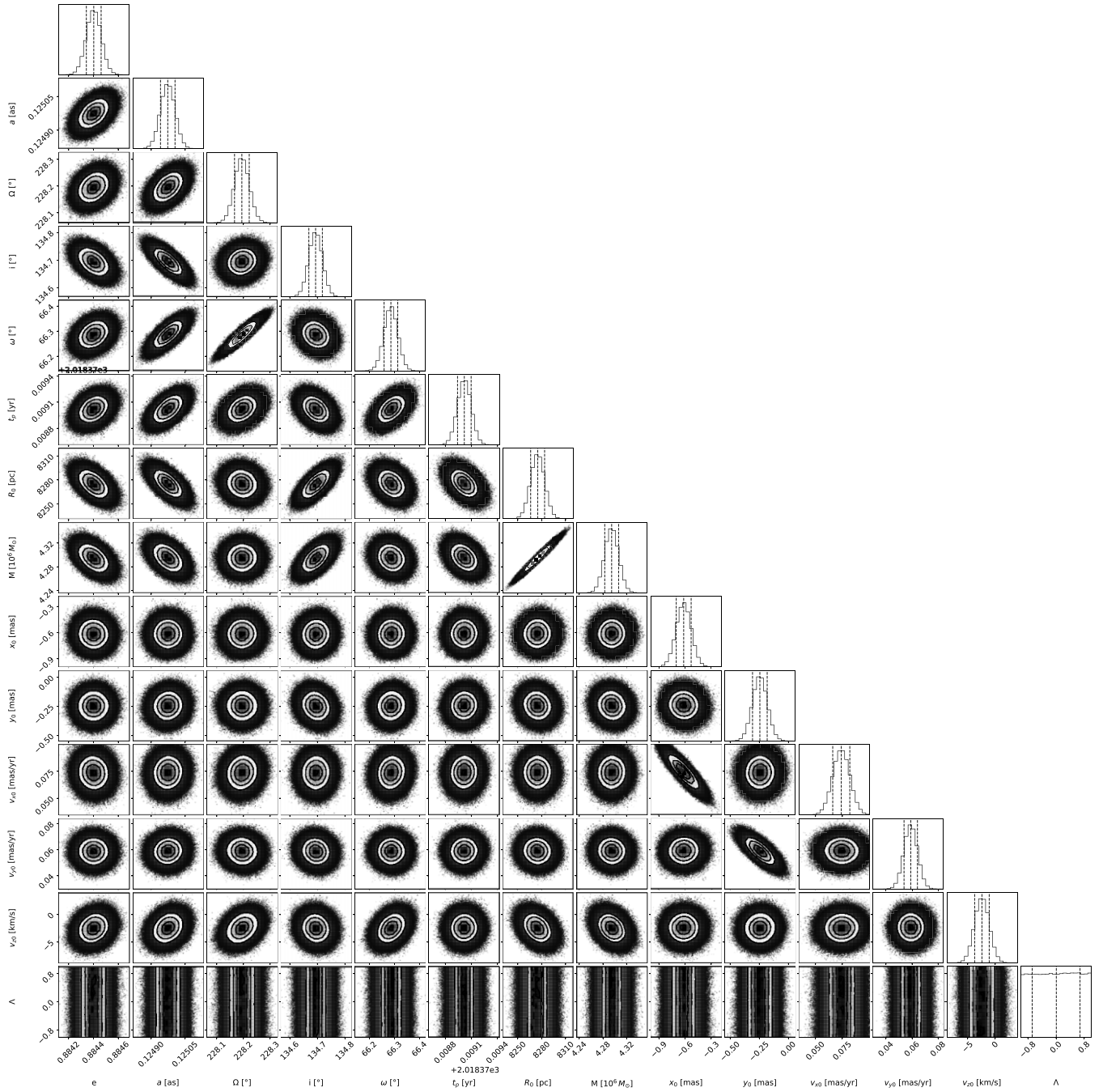
Figure C2. Corner plot of the fitted parameters with $f_{SP} = 1$ and $\alpha = 0.001$. Dashed lines represent the 0.16, 0.50, and 0.84 quantiles of the distributions.